1996

Limestone Characterization to Model Damage from Acidic Precipitation: Effect of Pore Structure on Mass Transfer

STEVE D. LEITH,[†]
MICHAEL M. REDDY,[‡]
W. FRED RAMIREZ,* AND
MICHAEL J. HEYMANS[§]

Department of Chemical Engineering, University of Colorado, Boulder, Colorado 80309-0424

The pore structure of Salem limestone is investigated, and conclusions regarding the effect of the pore geometry on modeling moisture and contaminant transport are discussed based on thin section petrography, scanning electron microscopy, mercury intrusion porosimetry, and nitrogen adsorption analyses. These investigations are compared to and shown to compliment permeability and capillary pressure measurements for this common building stone. Salem limestone exhibits a bimodal pore size distribution in which the larger pores provide routes for convective mass transfer of contaminants into the material and the smaller pores lead to high surface area adsorption and reaction sites. Relative permeability and capillary pressure measurements of the air/water system indicate that Salem limestone exhibits high capillarity and low effective permeability to water. Based on stone characterization, aqueous diffusion and convection are believed to be the primary transport mechanisms for pollutants in this stone. The extent of contaminant accumulation in the stone depends on the mechanism of partitioning between the aqueous and solid phases. The described characterization techniques and modeling approach can be applied to many systems of interest such as acidic damage to limestone, mass transfer of contaminants in concrete and other porous building materials, and modeling pollutant transport in subsurface moisture zones.

* Author to whom inquireies should be addressed; telephone: (303) 492-8660; fax: (303) 492-4341.

[†] Present address: University of Washington, Chemical Engr, Box 351750, Seattle, WA 98195.

[‡] Present address: U.S. Geological Survey—WRD, 3215 Marine Street, Boulder, CO 80303.

[§] Present address: Precision Core Analysis, 1338 South Valencia, Aurora, CO 80231.

Introduction

Acidic precipitation is an area of environmental concern in North America and other parts of the world. Most of the northeastern United States and parts of the upper Midwest, the Rocky Mountains, and the West Coast are subject to its effects (*1*). Many parts of Europe also report acidic precipitation effects. In addition to damaging the ecosystem, acidic precipitation takes its toll on widely used materials such as painted wood, metal, and carbonate stone (*2*). The financial consequences of this damage are difficult to assess, but estimates have placed the cost of prevention and remediation due to ambient sulfur and sulfate concentrations alone to be in the neighborhood of $2 billion (1982 dollars) per year (*3*). Other estimates claim that the direct costs of atmospheric corrosion in general and corrosion protection in industrial countries are on the order of 1−3% of the GNP (*4, 5*). Of considerable interest is the effect of acidic precipitation on building and dimension stone, such as limestone. Damage to limestone (and carbonate stone in general) by atmospheric SO_2 and NO_x has been well documented in the United States and Europe (*2, 6−15*).

The successful preservation of porous and permeable building stone exposed to acidic atmospheric environments hinges on the understanding of acidic precipitation deposition processes (i.e., wet and dry deposition) and damage mechanisms. Many investigators have attempted to describe damage mechanisms using empirical, electrochemical, and kinetic models but have been met with varying degrees of success (*12, 16−18*). Our approach is to formulate damage mechanisms based on moisture transport, in which wetting and drying of the stone drives dissolved contaminants from the stone surface through the pore network by diffusion and convection (*19, 20*).

The transport and accumulation of aqueous pollutants in the limestone interior is modeled based on the theory of variably saturated fluid flow in porous media (*21, 22*), a complex process influenced by the physical and chemical characteristics of the media, the contaminant, and the transport fluids. Mathematical description emerges from conservation of mass and the definition of the Darcy velocity (*20*). The concentration profile of a pollutant, c_i in fluid i is described by

$$\phi\frac{\partial c_i S_i}{\partial t} = \nabla(\phi S_i D_i \nabla c_i) - \nabla(c_i v_i) + r_i \qquad (1)$$

where v_i is the Darcy velocity of fluid i, ϕ is the porosity of the material, S_i is the pore volume saturation, and D_i is the diffusion coefficient of the pollutant in fluid i. The partitioning of contaminant between aqueous and solid phases is described by r_i, the net mass transfer rate of the pollutant into fluid i. The Darcy velocity of a fluid i is a function of fluid permeability and the pressure driving force for flow:

$$v_i = -\frac{k_{ei}}{\mu_i}\nabla(P_i + g\rho_i z) \qquad (2)$$

where μ_i is the viscosity of fluid i and k_{ei} is the effective permeability of the media to fluid i. The flow driving force is the combined term $P_i + g\rho_i z$ where P_i is the pressure in

fluid i, g is the gravitational acceleration, ρ_i is the density of fluid i, and z is the elevation. Both the effective permeability and fluid pressure are functions of the saturation, S_i. In addition to k_{ri} and P_i, r_i is the most important parameter in the model. Defining the correct mechanism for pollutant exchange between the phases, be it adsorption, precipitation, or heterogeneous reaction, greatly influences the interpretation and implications of the pore structure characterization.

Solution of the model eqs 1 and 2 requires application of appropriate boundary conditions (*20*) and determination of the functional relationships between fluid pressures, permeabilities, and phase saturations. Many researchers have formulated models relating the individual fluid saturations to fluid pressures and permeabilities (*23*–*26*), yet no model can fully account for the complexity and variability of an actual porous system (*27*). For this reason and to gain further insight into the physics of the present problem, comprehensive characterization of the limestone in terms of the pore structure and its effect on mass transfer is the focus of this work.

Materials and Methods

For this investigation, a block of beige, fossiliferous limestone was collected from near the top of the Mississippian Salem Formation at the Independent Quarry, near Bloomington, IN. The stone is graded as 'select buff', and the complete composition and mineralogy is detailed in refs 20 and 28. Mass transport-relevant characteristics were investigated in laboratories operated by the U.S. Geological Survey, Coors Brewing Co., and Marathon Oil Co. The capillary pressure function and optical analyses were investigated at U.S.G.S. facilities, while mercury intrusion porosimetry (MIP) and nitrogen adsorption measurements were made in cooperation with Coors. Analytical laboratories at the Marathon Oil Petroleum Technology Center were used to measure absolute and effective permeabilities and to determine the porosity of the stone.

Thin Section and Scanning Electron Microscopy Analysis. Thin sections were made from the Salem limestone with blue epoxy and rhodamine B fluorescent dye. Observation and photography of the thin sections was performed with a Nikon UFX-II polarizing microscope equipped with tungsten and mercury lamps and 35-mm camera. A representative section was chosen for illustrating the pore structure of this stone, and photographs were taken in series (at the same stage coordinates) at magnifications of 55× and 140×. Photographs of the sections in blue transmitted light and blue incident light were taken at each magnification. Pores appear dark blue when the section is viewed in blue transmitted light (blue filtered light from the tungsten lamp), fossiliferous limestone appears dark brown or black, and calcite cement appears white. The blue incident light was supplied by the mercury lamp, and the fluorescing pores appear green. The fluorescence reveals the micropores that cannot be seen when viewed in transmitted light.

Micrographs of limestone were taken using a Cambridge Stereoscan 250 Mk 2 scanning electron microscope (SEM). Compositional characterization of the sample surface was performed using energy dispersive X-ray (EDS) analysis. Limestone samples were observed and photographed at magnifications of 200× and 1250×.

Pore casts were made by impregnation of limestone billets with epoxy (identical to that used in thin section preparation) followed by etching in 0.1 M acetic acid. The limestone cast was submerged in acid until sufficient carbonate surface recession was observed (after about 1.5 weeks). Photographs of etched limestone pore casts were taken using an ISI XS-30 SEM, which was also equipped with EDS analysis software and hardware.

Mercury Intrusion and Nitrogen Adsorption Porosimetry. Mercury was incrementally forced into a limestone sample to successive states of static equilibrium using pressures ranging from 10 kPa to 411 MPa. The bulk density of the sample was 2.24 g/mL. The cumulative volume of mercury taken up by the stone was measured as a function of the applied pressure. Using the Young–Laplace equation (*29*), the pore entry radius corresponding to the applied pressure was calculated. The pore entry size distribution in the stone is illustrated by plots of cumulative and incremental intrusion volume against pore entry radius as described in the literature (*29, 30*).

In addition to determining the pore entry size distribution in the stone, MIP was used to quantify the pore surface area as well. By relating the work required to force an incremental volume of mercury into the pores of the limestone to the work required to form an area element of mercury/stone interface, it was possible to relate the pore surface area to pore volume (*29*). Plots of cumulative surface area and surface area distribution were made in an analogous manner to those for cumulative pore volume and pore entry size distribution.

The physical adsorption of a gas in the pore network of a solid was used to determine the pore size distribution of pores inaccessible by mercury intrusion (*29, 30*). Incremental measurements of the volume of nitrogen adsorbed by the sample as a function of relative pressure were used to determine a relationship between differential adsorbed nitrogen volume and pore radius via the Kelvin equation (*29, 30*). This common procedure was used to quantify the pore size and surface area distributions of the smallest limestone pores.

Capillary Pressure, Permeability, and Phase Saturation. A static method was used to determine the pressure/saturation relationship for air/water in Salem limestone (*31*). Two limestone blocks with dimensions of approximately 45 × 45 × 45 mm were fully saturated with water, and each was placed in a special pressure chamber. The total pore volume of each sample was determined by the measured difference between the dry weight of the sample and its wet weight when completely saturated with water of known density. The pressure chamber was designed with a water-permeable, ceramic plate serving as the base. Air was used to pressurize the vessel in an incremental range from 7 to 207 kPa. At each pressure increment, the air/water system in the limestone was allowed to reach hydrostatic equilibrium, with the air forcing the water out of the limestone pores, through the ceramic plate, and into a collection cylinder. At each equilibrium stage, the volume of displaced water was measured and recorded. Using the previously measured total pore volume, water saturations at the various pressure increments were calculated, and the capillary pressure curve was generated.

The absolute permeabilities of 11 cylindrical core plugs were determined using forced air flow. The porosity of each plug was determined by application of Boyle's law to helium gas infiltration. Relative permeabilities for air and water in the stone were measured in core plug no. 3. This

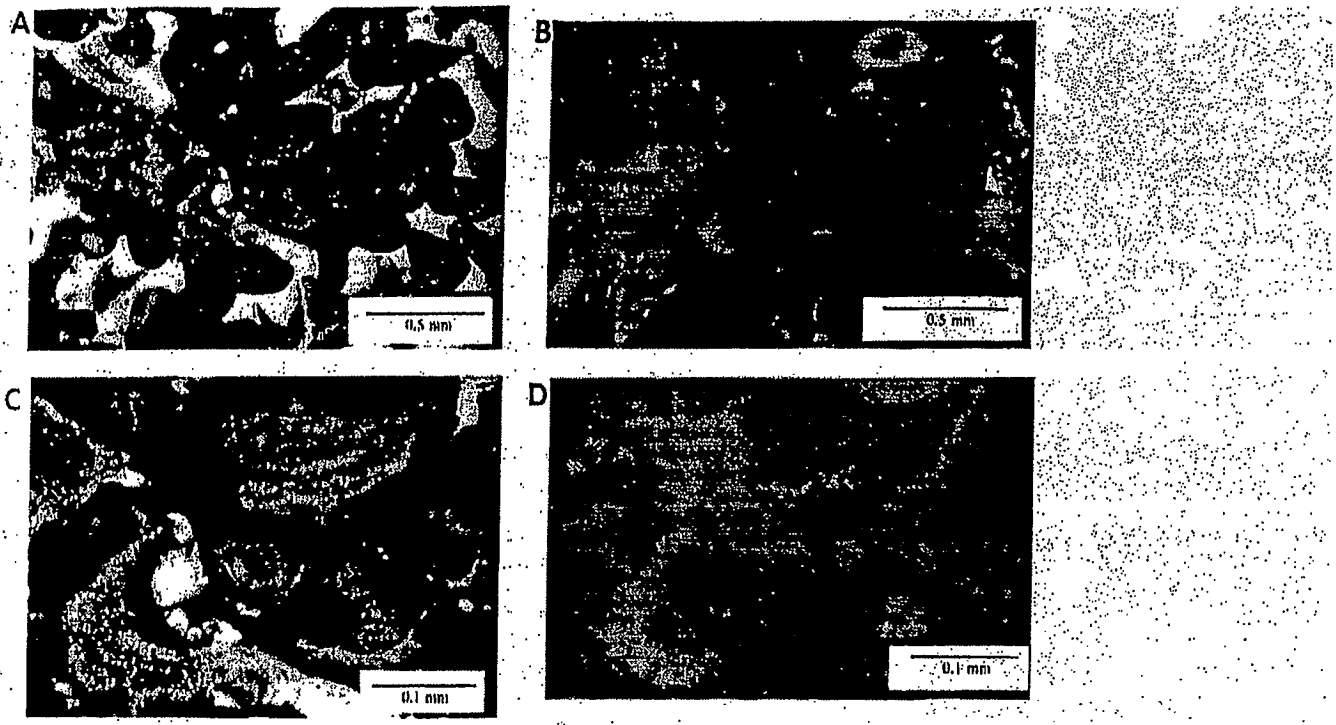

FIGURE 1. Salem limestone thin section in blue transmitted light (A and C) and blue incident light (B and D). Blue dye epoxy reveals the intergranular porosity between carbonate grains (A and C), and green epifluorescence indicates the presence of intragranular porosity within carbonate grains (B and D).

particular plug was chosen because it exhibited nearly the same porosity and permeability as the arithmetic average of the 11 core plug samples. No visible bedding laminations were observed in the core plug samples, and permeability measurements indicated a fairly high degree of homogeneity in the rock (porosities and air permeabilities were fairly uniform for all 11 core plugs).

The absolute permeability of cores 1–11 was determined by application of Darcy's law to air flow through the dry core using a CMS-300 permeameter manufactured by Core Labs. Each individual core was subjected to a radial net confining stress of 3445 kPa via a rubber core sleeve, and the axial flow of air was monitored as a function of applied pressure. Darcy's equation was used to relate permeability, air flow rate, and pressure drop. In practice, the actual permeability of the media may be less than the absolute air permeability measured in the cores at a given applied pressure due to slippage at the air/rock interface. Klinkenberg (*32*) was the first to address this phenomenon and how it relates to absolute permeability determination when using a gas flood method. He proposed a correction to account for the fluid/rock slippage, and it was used to determine the absolute permeability of the Salem limestone.

The relative permeability of a rock to a given fluid phase is commonly determined in a core sample by either steady-state, unsteady-state, or centrifuge methods (*31*, *33*). In the present study, the relative permeability of air and water in Salem limestone was measured using the unsteady-state method. With this method, one phase is displaced from the core by injection of the other. Using Buckley and Leverett's saturation front advancement theory (*34*), the relative permeability ratios were calculated by measurement of the produced fluid ratios (*31*), in this case air to water. When combined with the results from the absolute permeability measurements, the relative permeabilities allowed determination of the effective permeability/phase saturation relationship for air and water in the limestone.

Discussion of the capillary pressure and permeability requires definition of two important parameters. Consider the capillary pressure measurements made on the limestone samples. As air was forced into the water-saturated sample, the saturation of the water (S_W) decreased and eventually became independent of further increases in air pressure. This saturation is defined as the irreducible water saturation, S_{WO}. Similarly, upon water uptake by the dry samples, the air saturation decreased until the air phase became discontinuous. This saturation is defined as the residual air saturation, S_{AR}. Note that the water saturation under these conditions is $S_{WR} = 1 - S_{AR}$. The two parameters S_{WO} and S_{WR} are, therefore, end points for the range of saturations in which water can move by convection through the limestone.

Results and Discussion

Thin Section and SEM Analysis. Figure 1 shows photographs of the Salem limestone thin section in blue transmitted light and blue incident light. As evidenced by Figure 1A, a large pore network cross section with a diameter of about 0.25 mm is present. Its structure is dictated by the geometry of both the carbonate grains and calcite cement. Very fine pores cannot be distinguished. The same section, when viewed in blue incident light (Figure 1B), reveals that many fine pores are present within the carbonate grains. All that appears green is pore space occupied by the rhodamine-containing epoxy. Many of the carbonate particles are tinged with a light green hue. This indicates

the presence of very fine pores, although the size of these pores cannot be accurately determined at this magnification.

The thin sections in Figures 1C,D were taken at the same stage coordinates as those in Figure 1A,B, only at higher magnification (140×). Again, the large pores that appear blue in transmitted light, fluoresce green in blue incident light. Notice that the large carbonate structure at the top of the photograph exhibits little porosity when viewed in transmitted light but appears quite porous when photographed in blue incident light. The large pores are clearly seen in both pictures, while the very fine pores are visible only when viewed with epifluorescence. Even so, at this magnification, the area percentage of the fine pores cannot be precisely quantified. Although the size of a few pores can be estimated, the resolution is not high enough to allow exact quantification of pore size at this magnification. As almost the entire photograph appears as a shade of green, it is likely that very fine pores exist in the stone. The limits of fine resolution with a petrographic microscope, however, prevent direct observation of such pores.

Based on these thin section observations, Salem limestone appears to exhibit two kinds of porosity: intergranular and intragranular. The intergranular porosity is easily seen in transmitted light and is generally composed of larger pores. The intragranular porosity is easily seen when the sections are viewed in blue incident light. These pores, located within the fossil fragments and in the calcite matrix, are much smaller than the intergranular pores and likely contribute greatly to the total pore surface area.

Fluorescent thin section microscopy allows for a general observation of pores smaller than 1 μm in diameter, but individual pore structures and pore network details are too small to resolve petrographically. For this reason, scanning electron microscopy was used to study these smaller pores at higher magnification, while also offering a quasi-three-dimensional view of the carbonate grains and a partial view of the small, intragranular pore openings.

At 200× magnification (Figure 2A), small pore openings can be seen in bright areas of the micrograph. The size of these pores appear to be less than 5 μm, and their presence compliments the conclusions from the petrographic analysis. That is, a high degree of intragranular porosity appears to exist in the sample. At 1250× (Figure 2B), the location of the intragranular pores is illustrated further. The right half of Figure 2B is likely the rough surface of a sheared fossil fragment and appears to be comprised of particles less than 2 μm in size. Many pore openings can be identified in this region. The left side of Figure 2B appears to be calcite cement, but small pore openings are not easily seen at this magnification. Based on these observations and the results from the petrographic analysis, it seems that, of the intragranular pores, the very smallest are confined to the calcite cement. While the presence of these smaller pores is suggested by petrographic and conventional SEM analysis, examination of pore casts provides the most definitive view of the pore structure and location.

The etched limestone billets, when viewed with the SEM, clearly illustrate the complex pore structure of this stone. Since only the carbonate stone was susceptible to the acid etching, the epoxy pore cast represents the three-dimensional pore structure in which positive image represents pore volume and void space represents areas of zero porosity. The pore geometry is dictated by the shape and size of the voids in the limestone. These voids represent areas that were (before etching) either composed of calcite cement or grains of fossil fragments. Figure 3A–F was taken of the same sample at constant stage coordinates with magnification increasing from 25× to 1240×.

At 25× magnification (Figure 3A), the wide array of pore sizes in Salem limestone is illustrated. Notice what appears to be large cylindrical pores viewed in cross section in this figure. Many other pore geometries are observed as well. An estimate of the porosity by comparing the apparent volume of positive image to the void space suggests that the stone is considerably more porous than the measured average of 17.6%. In fact, concern existed as to the completeness of etching when these micrographs were first taken. It was thought that perhaps not all of the carbonate had been removed and that some carbonate or calcite cement was contributing to the positive image observed in the limestone billets. However, EDS verified that the positive image was composed entirely of epoxy and that complete etching had been achieved.

Figure 3B shows the sample at 50× magnification. The left side of the micrograph illustrates what appears to be a large, cylindrical pore in cross section and many other large macropores well over 100 μm in size. As the magnification increases, it becomes apparent that most of these seemingly large pores are actually comprised of many, very fine micropores. The micrographs shown in Figure 3C,D illustrate this for pores with an apparent radius of 50 μm. The last two micrographs in the series, Figure 3E,F, give some indication and appreciation of the size of the finer pores in the stone. Figure 3 suggests that both micropores and larger pores contribute considerably to the overall pore structure, although the micropores dominate in number. In addition, nearly all of the connected pores are a great deal smaller than the 10-μm scale in Figure 3F. The pore cast results are consistent with the results from the epifluorescence thin section investigations. That is, Salem limestone appears to be characterized by a wide range of pore sizes. Although the spatial distribution of the various pores types has been established qualitatively, the pore size frequency distribution cannot be easily determined from petrographic or conventional SEM methods. MIP and nitrogen adsorption methods provide a quantitative understanding of the pore structure in terms of volume and area distributions.

Mercury Intrusion and Nitrogen Adsorption Porosimetry. The pore entry size and pore surface area distributions in Salem limestone were determined by splicing the nitrogen adsorption and mercury intrusion results at a pore entry radius equal to 0.02 μm. Results are illustrated in Figures 4 and 5. The stone contains pores ranging in size from 0.001 to 35 μm, and the total cumulative pore volume for the sample measured was 0.132 mL/g. Note that over 99% of the total pore volume is attributable to pores with radii of 0.03 μm or larger and that the majority of the pore volume (54%) is contributed by pores with an entry radius $0.03 < r < 0.8$ μm. The petrographic study indicated that pores with radii much larger than 35 μm are present in the Salem limestone. The discrepancy between the optical and intrusion/adsorption results can be explained by the structure of the pore network.

It is common in limestone for large pores to be connected to the surface by small pores (*35*). This type of pore geometry is often referred to as "ink bottle" (*31, 35*). During intrusion measurements, mercury is only able to enter large pores at the much higher breakthrough pressure associated

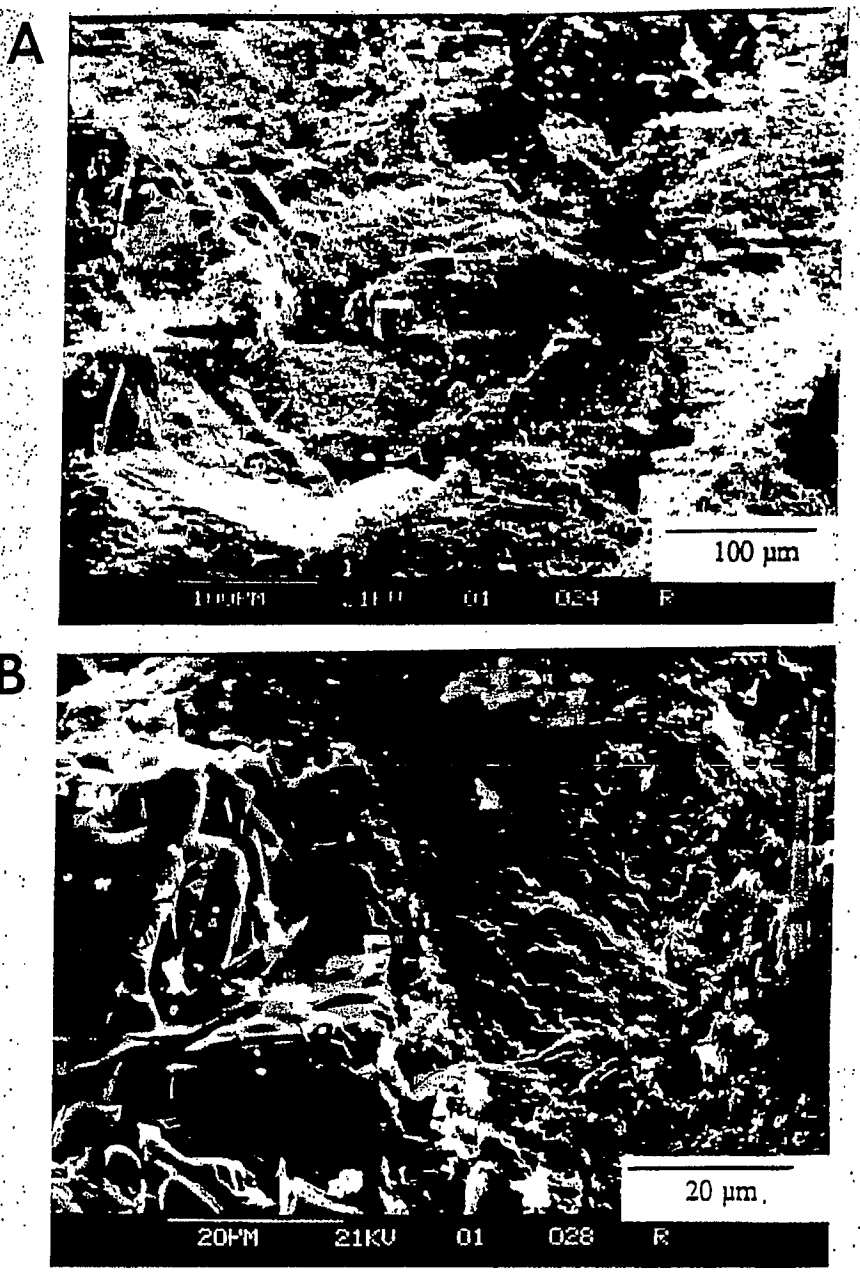

FIGURE 2. SEM micrographs of Salem limestone at (A) 200× and (B) 1250× magnification. Low magnification suggests the presence of intragranular porosity as indicated by the small openings in most of the grains shown. High magnification illustrates that pores within fossil fragments (right side) are larger than those in the calcite cement (left side).

with the small, connecting pores. This makes it difficult to directly determine the presence of large pores. In effect, mercury intrusion measures the radii of the connecting pores between the large, ink bottle pores. The result is that the large pores are hidden in the intrusion analysis.

The effective pore surface area was determined to be 1.51 m^2/g, and analysis of Figure 4 reveals that 70% of the total pore surface area is contributed by pores with radii of 0.03 μm and larger. Consider that pores of this size account for 99% of the total pore volume, and the significance of the fine pores is apparent. The 1% of the pore volume that is composed of mesopores and smaller contribute 30% of the total pore surface area in Salem limestone. The contribution to surface area of micropores ($r < 0.003\,\mu$m) alone is even more extreme. Although these very fine pores constitute only 0.18% of the total pore volume, they contribute 21% of the total pore surface area.

The pore entry size and pore area distributions are shown in Figure 5. Peaks appear at entry radii of 0.002 and 0.1 μm. The area under the pore entry size distribution curve is the volume of pore space contributed by pores of a given size. Analysis of Figure 5 indicates that nearly all of the pore volume in the Salem limestone is contributed by pores in two size ranges: $0.001 > r > 0.005\,\mu$m (the upper end of the micropore region) and $0.01 > r > 0.3\,\mu$m (primarily the macropore region). It has been found in catalysts having a bimodal pore size distribution that the fine pores are often in the size range $0.001 > r > 0.01\,\mu$m, and these small

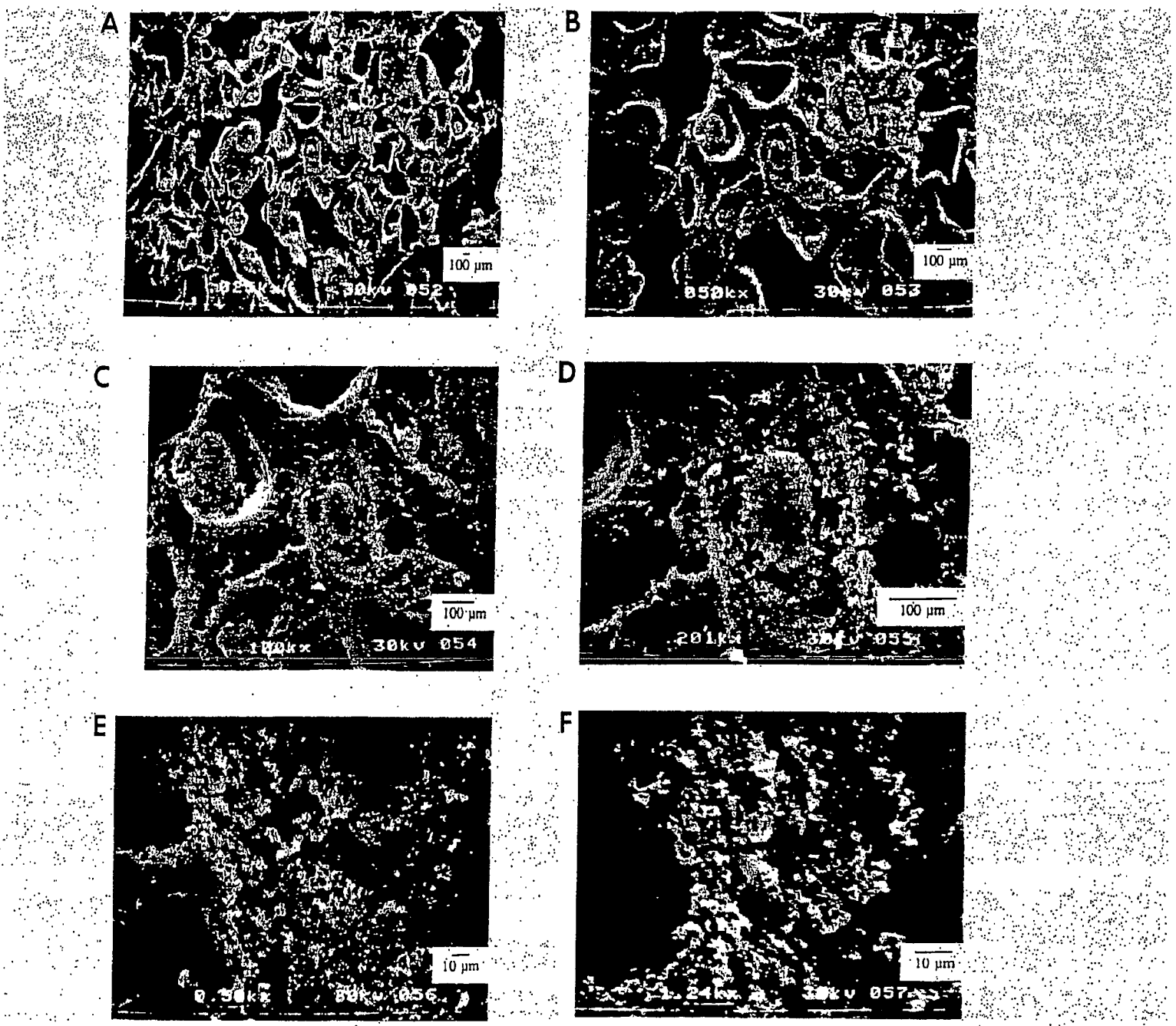

FIGURE 3. SEM micrographs of Salem limestone pore casts. Positive image represents the porosity in the sample, and void space illustrates the location of nonporous carbonate material removed by etching with acetic acid.

pores account for most of the pore surface area (*36*). Note that a high percentage of the total pore surface area in Salem limestone is contributed by the fine pores with entry radii less than 0.01 μm. In catalysts that exhibit such a pore geometry, the larger pores can provide rapid mass transfer into the sample, from which the fine pores can lead to reaction sites or be reaction sites themselves (*36*). It is likely that transport and reaction of aqueous pollutants in the limestone may be affected in a similar way due to the bimodal character of the pore size distribution and the large contribution to surface area by the smallest pores. That is, contaminants may be convected primarily through the large mesopores and macropores while the precipitation and/or reaction of pollutants may take place nearly exclusively in the fine pore structure.

Capillary Pressure, Permeability, and Phase Saturation. Results from the porous plate capillary pressure measurements are illustrated in Figure 6. The curve represents the average pressure/saturation behavior of the two limestone samples investigated. Since the stones were vacuum saturated, the residual air saturation, S_{WR}, cannot be determined from this curve but must be approximated by the permeability measurements. The irreducible water saturation, S_{WO}, is approximated by the asymptotic behavior of the capillary pressure curve. It appears that the water saturation approaches a value not much less than 0.60 upon

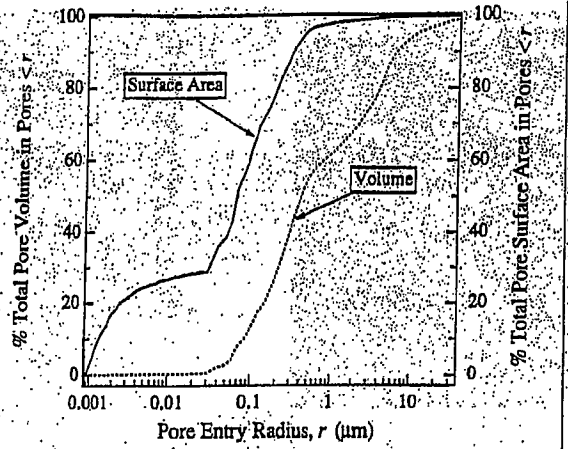

FIGURE 4. Salem limestone pore entry size and pore surface area distributions as determined by mercury intrusion and nitrogen adsorption. Note that only 1% of the pore volume is contributed by pores with radii of 0.03 μm and smaller, but these small pores contribute 30% of the total surface area.

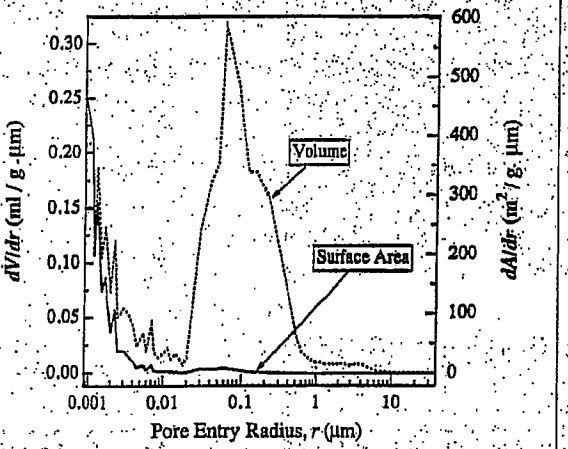

FIGURE 5. Salem limestone pore entry size and pore surface area distributions as determined by mercury intrusion and nitrogen adsorption. Note the bimodal nature of the pore entry size distribution and the large percentage of surface area contributed by the smallest pores.

application of increasing air pressures. We assume here that this is the irreducible saturation, and analysis of the relative permeability curves confirms that $S_{wo} = 0.60$ is a good approximation.

The physical significance of the capillary pressure function lies in the high irreducible water saturation and its relationship to the pore size distribution in Salem limestone. The capillary pressure function illustrates that, once wet, the limestone will not easily give up retained moisture. In fact, 60% of the pore volume remains water-saturated regardless of increasing air pressure through the stone. This is explained by the existence of a significant pore volume contributed by pores of small entry radii. These smaller pores imbibe and hold water by capillarity, and the implications to moisture and solute transport through the pore network are extremely important. As this strongly held pore water is immobile, moisture transport must occur by evaporation/condensation mechanisms, and contaminant transport must occur by diffusive processes alone. Only when the stone is greater than 60% water-saturated will convective transport mechanisms be significant.

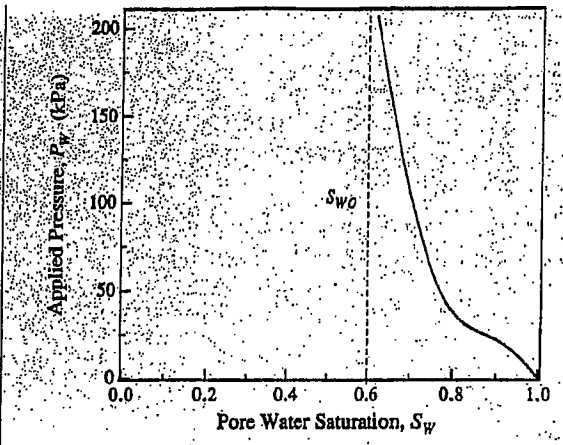

FIGURE 6. Capillary pressure curve for air/water in Salem limestone as determined by static measurements of moisture loss in a pressure chamber. The irreducible water saturation is approximately 0.60, indicating that at low saturations water is held tightly by capillarity and is immobile.

TABLE 1

Salem Limestone Core Plug Analysis[a]

sample no.	core diameter (cm)	core length (cm)	pore vol (mL)	porosity	permeability ($cm^2 \times 10^{10}$)
1	2.527	7.397	6.478	0.174	1.156
2	2.528	7.560	6.628	0.175	1.136
3	2.528	7.483	6.587	0.174	1.381
4	2.528	7.422	6.520	0.175	0.977
5	2.528	7.451	6.463	0.171	1.146
6	2.531	7.585	6.906	0.181	1.665
7	2.527	7.426	6.722	0.179	1.438
8	2.531	7.438	6.608	0.177	1.235
9	2.530	7.617	6.743	0.175	1.606
10	2.530	7.348	6.539	0.176	1.620
11	2.530	7.427	6.646	0.178	1.410
av	2.529	7.47	6.62	0.176	1.34
95% confidence interval	±0.001	±0.05	±0.08	±0.002	±0.13

[a] Porosity was determined by application of Boyle's law to helium gas infiltration and permeability by the gas flood method with Klinkenberg correction.

The arithmetic average porosity of the 11 core plug samples was determined to be 17.6% with porosities ranging from 17.3 to 18.1%. Porosity of limestone used as building material can vary from 5 to 20% (*37*). The permeabilities (corrected for the Klinkenberg effect) ranged from 9.8×10^{-11} cm^2 to 1.65×10^{-10} cm^2 for the 11 cores with the average being 1.34×10^{-10} cm^2. Permeabilities of building and monument limestone are commonly in the range 1.0×10^{-12}–6.0×10^{-9} cm^2 (*37*). The sample permeabilities and porosities are summarized in Table 1.

The relative permeability curves are illustrated in Figure 7. Laboratory measurements of relative permeability often exhibit a dependence on the saturation history of the media and hysteresis between the wetting and drying curves (*27, 31*). The hysteresis is thought to be caused by complex pore geometries, contact angle hysteresis, and nonwetting fluid entrapment, although other factors may contribute as well. Correct interpretation of the permeability/saturation relationship requires definition of the relative permeability ratio, k_r, for both stone drying and wetting mea-

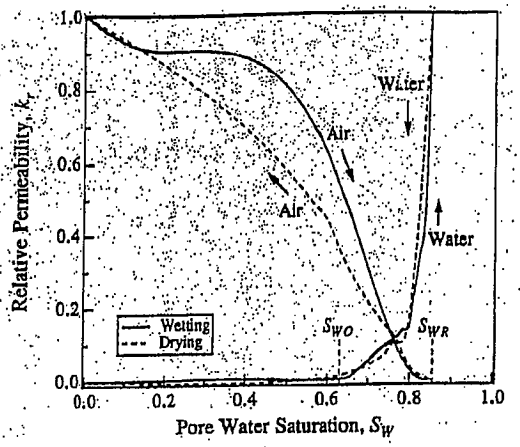

FIGURE 7. Relative permeability curves for air and water in Salem limestone as measured using unsteady-state, forced-flow techniques. Wetting curves are denoted by solid lines (—), and drying curves are denoted by dashed lines (---). Note for wetting curves $k_r = k_e/k_a$ and for drying curves $k_r = k_e/(kS_{WR})$. The absolute permeability to air, k_a, was determined by forced air flow through a sample core (Table 1).

surements. By convention, k_r is defined for the wetting curves as the effective permeability, k_{ei}, divided by the absolute permeability to air, k_a, where i represents either the air or water phase. For the drying curves, k_r is defined as the ratio of k_{ei} to the effective permeability at the residual water saturation, k_{SWR}. Information from the curves is used in two ways. First, a quantitative description of the water/air transport mechanisms in the stone is illustrated. Second, the relative permeability curves can be used to determine the functional relationship between k_{ei} and S_i needed to solve the mass transfer eqs 1 and 2.

Analysis of the wetting curves (solid lines in Figure 7) indicates that pore water will not flow through the limestone until a water saturation of nearly 0.65 is reached. At saturations less than this value, water will imbibe into the stone, but once there is held strongly by capillarity in the fine pores and is immobile. At saturations greater than 0.65, the water has formed a continuous phase through a portion of the pore network, enabling the applied pressure to influence the water distribution in the stone.

The maximum water permeability occurs at $S_{WR} = 0.85$, which corresponds to a residual air saturation of 0.15. These results imply that 15% of the pore volume is always air filled and has no effect on water movement through the stone. Based on the porosimetry measurements and the ink bottle nature of the limestone pore structure, it is likely that the air is trapped in large pores by water-filled, connecting pores. These isolated ink bottles do not contribute to effective permeability at this saturation because the network of smaller, continuous pores provides the vast majority of pathways for water movement.

Analysis of the drying curves (dashed lines in Figure 7) indicates that the relative permeability of water decreases rapidly from 1.0 to nearly zero below a water saturation of 0.60. Below this saturation, the water is held tightly by capillarity and is immobile irrespective of further increases in applied air pressure. Note that for water saturations less than 0.60, the air and water drying curves presented here cannot be determined by conventional forced-flow measurements. Instead, these curves represent inferred extrapolation of the data expected for drying by evaporation.

Both the wetting and drying curves suggest that, once the stone is wet, water is held tightly in the pore network and, except in the region of $0.60 < S_W < 0.85$, water will not exit the stone by convective processes. Rather, evaporation is likely to be a significant process by which water is removed at water saturations below 0.60. In addition, the most likely transport mechanism for contaminants at $S_W < 0.60$ is diffusion while both convective and diffusive transport will be significant in the water saturation range $0.60 < S_W < 0.85$.

Conclusions

The influence of pore structure on flow characteristics and solute transport in Salem limestone is apparent through analysis of the pore size and pore area distributions and their relationship to overall porosity. As measured using helium gas infiltration, the limestone porosity was found to be 17.6%. Thin section and SEM analyses indicate that porosity is primarily of inter- and intragranular nature, although a majority of the pore volume is contained within the carbonate grains. Further quantitative assessment by nitrogen adsorption and MIP reveals that the stone exhibits a bimodal pore size distribution, and a significant portion of the pore surface area is contained in the smallest pores.

The results from the relative permeability measurements and capillary pressure function reported here compliment and are consistent with the findings from the stone characterization. The data indicate that Salem limestone has a very low effective permeability to water, even at high water saturations. This can be explained by the existence of many small pores that hold high volumes of static water, while in the larger pores water is easily displaced by air. It is possible for the water saturations to be relatively high (due to the small pores) while the flow of water is virtually zero (due to the air-filled, large pores). The stone exhibits an irreducible water saturation of around 0.60. Therefore, more than half of the stone pore volume can be filled with static water. This implies that in wet limestone, the transport of pollutants through the aqueous phase is going to be restricted to nonconvective (diffusive) mechanisms for water saturations less than 0.60.

Another significant relationship between pore structure and contaminant transport in limestone concerns the location of surface area. The surface area distribution reveals that a large portion of the stone surface area is contained in micropores, i.e., those more apt to contain water. The result is that a large number of surface sites will be accessible for adsorption and reaction with aqueous pollutants in these wetted pores.

Of specific interest is the effect of pore structure on stone damage. The pore structure analysis suggests that stones exposed to ambient conditions will likely become wet (by rain or condensation) and will partially dry (by gravitational drainage or evaporation) depending on the cycles of humidity exposure. The characterization of the limestone pores indicates that large ink bottle pores will be the last to fill with water and the first to dry. The accumulation of pollutant in the material will depend on the mechanism of partitioning defined in the transport equation. If adsorption and heterogeneous reaction are probable mechanisms, then the small, high surface area pores will be more vulnerable to chemical alteration by contaminants. If precipitation and crystal growth are the primary mechanisms for pollutant exchange, the larger pores will accumulate the

contaminant to a greater extent due to repeated wetting and drying.

The qualitative optical analysis, in conjunction with the quantification of pore size distribution, permeabilities, and capillary pressure function, aids in the evaluating and understanding of transport mechanisms in variably saturated Salem limestone. Once characterized, these parameters can help form the basis for successfully modeling mass transport of contaminants in limestone buildings and monuments exposed to acidic environments. In addition, the characterization techniques and modeling approach described here can be applied to many other systems of interest such as mass transfer in concrete and other porous building materials and modeling of contaminant transport in subsurface moisture zones.

Acknowledgments

We thank Marathon Oil Company for drilling the limestone core plugs and measuring porosity and permeabilities. The U.S. Geological Survey provided financial support for this research project and use of their SEM facility. Rick Healy of the U.S.G.S. provided valuable assistance in the determination of the capillary pressure function. Phil Harding at the University of Washington is thanked for many helpful discussions.

Literature Cited

(1) Glass, N. R.; Arnold, D. E.; Galloway, J. N.; Hendrey, G. R.; Lee, J. J.; McFee, W. W.; Norton, S. A.; Powers, C. F.; Rambo, D. L.; Schofield, C. L. *Environ. Sci. Technol.* **1982**, *16*, 162A–169A.

(2) Baedecker, P. A.; Edney, E. O.; Moran, P. J.; Simpson, T. C.; Williams, R. S. In *NAPAP Report 19, Acidic Deposition: State of Science and Technology*; National Acid Precipitation Assessment Program: Washington, DC, 1990; 19-1–19-280.

(3) Lareau, T. J.; Horst, R. L.; Manuel, E. H.; Lipfert, F. W. In *Materials Degradation Caused by Acid Rain*; Baboian, R., Ed.; ACS Symposium Series 318; American Chemical Society: Washington, DC, 1986; pp 397–410.

(4) Gellings, P. J. *Introduction to Corrosion Prevention and Control*; Delft University Press: Delft, 1985.

(5) Passaglia, E. In *Materials Degradation Caused by Acid Rain*; Baboian, R., Ed.; ACS Symposium Series 318; America Chemical Society: Washington, DC, 1986; pp 384–396.

(6) Haynie, F. H. *Durability Build. Mater.* **1983**, *1* (3), 241–254.

(7) Winkler, E. M. *Environ. Geol. Water Sci.* **1987**, *9* (2), 85–92.

(8) Cheng, R. J.; Hwu, J. R.; Kim, J. T.; Leu, S. M. *Anal. Chem.* **1987**, *59* (2), 104A–106A.

(9) Reddy, M. M. *Earth Surf. Processes Landforms* **1988**, *13*, 335–354.

(10) Yocom, J. E. *J. Air Pollut. Control Assoc.* **1979**, *29* (4), 333–338.

(11) Skoulikidis, T.; Papakonstantinou-Ziotis, P. *Br. Corros. J.* **1981**, *16* (2), 63–69.

(12) Skoulikidis, T.; Charalambous, D.; Papakonstantinou-Ziotis, P. *Br. Corros. J.* **1983**, *18* (4), 200–202.

(13) Trudgill, S. T.; Viles, H. A.; Cooke, R. J.; Inkpen, R. J.; Heathwaite, A. L.; Houston, J. *Atmos. Environ.* **1991**, *25A* (12), 2851–2853.

(14) Schiavon, J. *Ean. Cult. Her.* **1992**, *6* (3), 35–46.

(15) Gauri, K. L.; Kulshreshtha, N. P.; Punuru, A. R.; Chowdhury, A. N. *J. Mater. Civ. Eng.* **1989**, *1* (2), 73–85.

(16) Lipfert, F. W. *Atmos. Environ.* **1989**, *23* (2), 415–429.

(17) Kulshreshtha, N. P.; Punuru, A. R.; Gauri, K. L. *J. Mater. Civ. Eng.* **1989**, *1* (2), 60–72.

(18) Tambe, S.; Gauri, K. L.; Suhan, L.; Cobourn, W. G. *Environ. Sci. Technol.* **1991**, *25*, 2071–2075.

(19) Reddy, M. M.; Leith, S. D. *Preprints of Papers*, 205th National Meeting of the American Chemical Society—Division of Environmental Chemistry; Denver, CO; American Chemical Society: Washington, DC, 1993; pp 43–46.

(20) Leith, S. D. M.S. Thesis, University of Colorado at Boulder, 1993.

(21) Bear, J.; Bachmat, Y. In *Fundamentals of Transport Phenomena in Porous Media*; Bear, J., Corapcioglu, M., Eds.; Marinus Nijhoff: Dordecht, 1984.

(22) Bear, J.; Verruijt, A. *Modeling Groundwater Flow and Pollution*; D. Reidel: Dordecht, 1987.

(23) Brooks, R. H.; Corey, A. T. *Hydraulic properties of porous media*; Hydrology Paper 3; Colorado State University: Ft. Collins, CO, 1964.

(24) van Genuchten, M. T. *Soil Sci. Am. Proc.* **1980**, *44* (5), 892–898.

(25) Haverkamp, R.; Parlange, J. *Soil Sci.* **1983**, *142*, 325–339.

(26) Lenhard, R. J.; Parker, J. C. *Water Resour. Res.* **1987**, *23*, 2197–2206.

(27) Parker, J. C. *Rev. Geophys.* **1989**, *27* (3), 311–328.

(28) McGee, E. S. In *NAPAP Report 19, Acidic Deposition: State of Science and Technology*; National Acid Precipitation Assessment Program: Washington, DC, 1990; pp 19-107–19-108.

(29) Gregg, S. J.; Sing, K. S. *Adsorption, Surface Area and Porosity*, 2nd ed.; Academic: New York, 1982.

(30) Satterfield, C. *Heterogeneous Catalysis in Industrial Practice*, 2nd ed.; McGraw-Hill: New York, 1991.

(31) Dullien, F. A. *Porous Media: Fluid Transport and Pore Structure*; Academic: New York, 1979.

(32) Klinkenberg, L. *Drilling and Production Practices*; Academic: Orlando, 1941.

(33) Honorpour, M.; Koederitz, L.; Harvey, A. *Relative Permeability of Petroleum Reservoirs*; CRC: Boca Raton, FL, 1986.

(34) Buckley, S. E.; Leverett, M. C. *Trans. AIME* **1942**, *146*, 107–116.

(35) Punuru, A. R.; Chowdhury, A. N.; Kulshreshtha, N. P.; Gauri, K. L. *Environ. Geol. Water Sci.* **1990**, *15* (3), 225–232.

(36) Satterfield, C. *Heterogeneous Catalysis in Industrial Practice*, 2nd ed.; McGraw-Hill: New York, 1991.

(37) Domenico, P. A.; Schwartz, F. W. *Physical and Chemical Hydrogeology*; Wiley: New York, 1990.

Received for review August 8, 1995. Revised manuscript received February 7, 1996. Accepted February 26, 1996.[⊗]

ES950583Q

[⊗] Abstract published in *Advance ACS Abstracts*, XxxxxxxxYY, ZZZZ.